Nightside ionosphere of Mars: Modeling the effects of crustal magnetic fields and electron pitch angle distributions on electron impact ionization

Robert J. Lillis,[1] Matthew O. Fillingim,[1] Laura M. Peticolas,[1] David A. Brain,[1] Robert P. Lin,[1] and Stephen W. Bougher[2]

Received 13 March 2009; revised 10 July 2009; accepted 3 August 2009; published 20 November 2009.

[1] The night side ionosphere of Mars is known to be highly variable: essentially nonexistent in certain geographic locations, while occasionally nearly as strong as the photoionization-produced dayside ionosphere in others. The factors controlling its structure include thermospheric densities, temperatures and winds, day-night plasma transport, plasma temperatures, current systems, solar particle events, crustal magnetic fields, and electron precipitation, none of which are adequately understood at present. Using a kinetic Monte Carlo approach called Mars Monte Carlo Electron Transport (MarMCET), we model the dynamics of precipitating solar wind electrons on the nightside ionosphere of Mars to study the effects of these last two factors on ionospheric density and structure. We calculate ionization rate profiles and, using simple assumptions concerning atmospheric chemistry, also calculate electron density profiles, total electron content, and equivalent ionosphere slab thickness. We present the first model investigation of the coupled effects of crustal magnetic field gradients and precipitating electron pitch angle distributions (PADs). Including such effects, particularly in cases of nonisotropic PADs, is found to be essential in accurately predicting ionization rate and electron density profiles: peak ionization rates can vary by a factor of 20 or more when these effects are included.

Citation: Lillis, R. J., M. O. Fillingim, L. M. Peticolas, D. A. Brain, R. P. Lin, and S. W. Bougher (2009), Nightside ionosphere of Mars: Modeling the effects of crustal magnetic fields and electron pitch angle distributions on electron impact ionization, *J. Geophys. Res.*, *114*, E11009, doi:10.1029/2009JE003379.

1. Introduction

1.1. Mars' Dayside Ionosphere

[2] The dayside ionosphere of Mars is primarily the result of photoionization of atmospheric neutrals by solar EUV flux, with a vertical structure and solar zenith angle (SZA) dependence that is described reasonably well by classical Chapman theory [*Chapman*, 1931a, 1931b]. Since 2001, more than two dozen publications on the Mars dayside ionosphere have appeared, primarily using data from the Radio Science (RS) experiment on Mars Global Surveyor (MGS) [*Tyler et al.*, 2001] and the Mars Advanced Radar for Surface and Ionospheric Sounding (MARSIS) on Mars Express [*Gurnett et al.*, 2005]. Departures from ideal Chapman behavior have been studied and attributed to the omission of plasma transport, comprehensive ion chemistry and vertical diffusion in the Chapman model [e.g., *Breus et al.*, 2004; *Fox and Yeager*, 2006].

[3] The variability of the dayside ionosphere is caused by external drivers such as the solar cycle, solar rotation [*Breus et al.*, 2004; *Withers and Mendillo*, 2005], solar flares [*Mendillo et al.*, 2006], cosmic rays [*Molina-Cuberos et al.*, 2001, *Haider et al.*, 2007] gamma ray bursts [*Espley et al.*, 2008] and solar energetic particle (SEP) events [*Morgan et al.*, 2008; *Espley et al.*, 2007] and internal factors such as neutral density variations [*Bougher et al.*, 2001], crustal magnetic fields and local plasma processes [*Withers et al.*, 2005; *Duru et al.*, 2006; *Nielsen et al.*, 2007]. *Withers* [2009] provides a comprehensive review of observations of the dayside ionosphere to date.

1.2. Mars' Nightside Ionosphere

[4] In contrast, our understanding of the nightside ionosphere remains substantially incomplete, with very little published data compared to the dayside. The nightside ionosphere does not start at solar zenith angle (SZA) = 90° because ionospheric altitudes (say, 100 km to 200 km) are sunlit for SZA < ∼105°–110°. Ionospheric plasma was only detected in 60% of Viking radio occultation profiles between SZA = 90° and 125° [*Zhang et al.*, 1990], of which the average peak electron density was 5×10^3 cm^{-3}, which is a factor of ∼20–40 below subsolar values [*Gurnett et al.*, 2008]. Earth-Mars geometry prevents radio occultation measurements at SZAs above 125°. Though MARSIS nightside observations have been made up to SZA = 140° (O. Witasse, personal communication, 2009), this data is not

[1]Space Sciences Laboratory, University of California, Berkeley, California, USA.
[2]Department of Atmospheric, Oceanic and Space Sciences, University of Michigan, Ann Arbor, Michigan, USA.

0148-0227/09/2009JE003379

public at the time of writing and data in published articles have been limited to SZA < ~115°. Nonetheless, for SZA > ~100°, *Gurnett et al.* [2008] reported "irregular patches" of ionosphere, with higher peak densities occurring in areas of strong crustal magnetic fields. Also for SZA > 100°, *Safaeinili et al.* [2007] reported higher peak densities specifically where the crustal magnetic fields were closer to vertical than horizontal. This irregularity and correlation with crustal fields is consistent with some combination of electron impact ionization, transport from the dayside and dynamic magnetic field topology, together controlling the nightside ionosphere. Oddly, there are no published nightside studies from either the MGS or Mars Express Radio Science experiments. Overall, the near-terminator nightside ionosphere is highly variable and is not well understood, while the deep nightside ionosphere (SZA = 125°–180°) remains completely unexplored [*Withers*, 2009].

[5] The factors that control the spatial and temporal behavior of the nightside ionosphere are expected to be:

[6] 1) Neutral densities, temperatures, winds and waves [e.g., *Bougher et al.*, 1999; *Withers et al.*, 2003],

[7] 2) Day-night plasma transport [e.g., *Ulusen and Linscott*, 2008],

[8] 3) Ablation by meteoroid influx [*Withers*, 2009],

[9] 4) Recombination rates, which depend upon electron temperature [e.g., *Schunk and Nagy*, 2000],

[10] 5) Transient SEP [*Leblanc et al.*, 2002] or gamma ray burst events [*Espley et al.*, 2008],

[11] 6) Magnetic field-aligned electrostatic potential drops, which may arise at and above ionospheric altitudes [e.g., *Dubinin et al.*, 2008],

[12] 7) Impact ionization by precipitating superthermal magnetotail electrons, and hence those electrons' energy spectra and pitch angle distributions (PADs) [e.g., *Brain et al.*, 2006],

[13] 8) Magnetic field strength and topology, which varies with time because the often strong planet-fixed crustal magnetic fields reconnect with the draped and time-variable interplanetary magnetic field (IMF) as Mars rotates [e.g., *Halekas et al.*, 2006].

[14] Data remain sparse concerning factor 1 [e.g., *Withers*, 2006]. Factors 2–6 remain substantially unknown due to lack of reliable data, though the upcoming 2013 MAVEN Mars Scout (http://lasp.colorado.edu/maven/) mission should make many of these measurements. This work focuses on the last two factors.

1.3. Previous Modeling Efforts

[15] Several investigators have previously modeled electron transport through the Mars upper atmosphere. Such studies vary in approach from a simple analytic model [*Verigin et al.*, 1991], multistream models [*Haider et al.*, 1992; *Fox et al.*, 1993; *Fillingim et al.*, 2007], a kinetic and fluid model [*Leblanc et al.*, 2006], an analytic yield spectrum approach [*Haider*, 1997; *Seth et al.*, 2002; *Haider et al.*, 2002]. These models have been used to study ionization rates [*Haider et al.*, 2002; *Fillingim et al.*, 2007], auroral emissions [*Seth et al.*, 2002], atmospheric chemistry [*Haider*, 1997; *Haider et al.*, 2007] and expected Mars nightside ionospheric electron density profiles [e.g., *Fox et al.*, 1993]. These models have been used to examine the effects of different energy spectra of precipitating electrons under different atmospheric conditions, but to date have not included magnetic field gradients, nor anisotropic pitch angle distributions of the precipitating electrons.

1.4. Effects of Crustal Fields, Electron PADs, and Energy Spectra

[16] In this work we attempt to examine how crustal magnetic fields, electron energy spectra and electron PADs (for all three of which there is a reasonable base of data from which to start) affect the nightside ionosphere of Mars. These factors are connected, in that the topology of the crustal magnetic field, combined with the double-lobed Martian magnetotail field [e.g., *Ferguson et al.*, 2005], strongly affects where, when and how superthermal electrons can precipitate into the atmosphere and cause ionization. For instance, where magnetic field lines are "open" (i.e., they connect the collisional atmosphere to the IMF), magnetotail electrons have access to, and hence can impact, the atmosphere. In contrast, where such field lines are "closed" (i.e., connected to the planet at both ends) above collisional altitudes (i.e., >~200 km) or "unconnected" (i.e., unconnected to the atmosphere), magnetotail electrons have no such access. Maps showing the locations of these "regions of access" (and hence ionization) at ~400 km altitude can be found in the works of *Lillis et al.* [2008a, Figure 1b] and *Brain et al.* [2007, Figure 5f].

[17] No previous electron impact ionization modeling effort at Mars has included an inhomogeneous magnetic field, nor its interplay with the PADs of the precipitating electrons, and simulated how these effects modify vertical profiles of ionization rate. Crustal magnetic field gradients, which are included in this study, are potentially important on Mars because field strengths vary rapidly with altitude unlike Earth or any planet with a global magnetic field generated in its deep interior.

[18] In section 2, we describe the Mars Monte Carlo Electron Transport (MarMCET) code and how we use it to calculate vertical profiles of ionization rate and electron density. In section 3 we present the first modeling results showing how predicted vertical ionization rate varies as a function of crustal magnetic field strength and PAD. In section 4, we compare our results to previous observations and modeling efforts. Section 5 discusses conclusions and future work.

2. Methodology

2.1. Mars Monte Carlo Electron Transport Code

[19] MarMCET takes a kinetic, Monte Carlo approach to electron motion in a planetary atmosphere and is described in detail in sections 3–5 of *Lillis et al.* [2008b]. The following summary is adequate for its use as a tool to study ionization.

[20] Individual electrons start with a given altitude, pitch angle α_0 and energy U_0 and are assumed to be traveling downward toward the planet. The magnetic field at this initial point is denoted B_0. Since the gyroradii of <20 keV electrons on the Martian nightside is always <25 km (and often much smaller), we assume the electron remains "bound" to the magnetic field line. The collection of points (i.e., loci) about which an electron gyrates in its helical motion is commonly known as the guiding center path or distance along the field line [*Parks*, 2004, pp. 118–121] and is represented by the

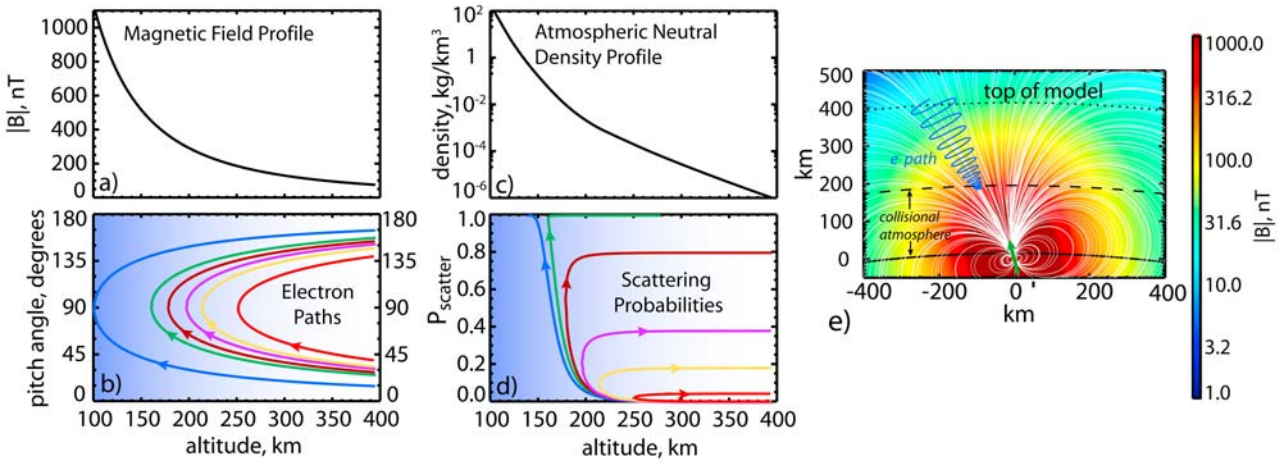

Figure 1. (a) A typical magnetic field-altitude profile for a region of strong crustal field and (b) the pitch angle evolution which this profile dictates for electrons starting at 400 km altitude at six different pitch angles: 15, 24, 27, 30, 33, and 40 degrees (i.e., the pitch angle at the lower right end of each line) in the absence of any electrostatic potential. (c) A typical mass density-altitude profile and (d) the resulting cumulative scattering probabilities for the same electron paths in Figure 1b for 200 eV electrons as they travel down in altitude and back up again. (e) A two-dimensional illustration showing the magnetic topology of an open crustal magnetic field line region, the helical path of precipitating electrons, the top of our model (400 km), and approximate altitude range of the collisional atmosphere. The green arrow represents the direction of crustal magnetization. In Figures 1b and 1d, arrows show the electrons' direction of motion while the gradient in light blue color from right to left approximately represents atmospheric density as a function of altitude and is meant as a visual aid to demonstrate that electrons with initial pitch angles further from 90° encounter higher atmospheric densities and are therefore more likely to scatter. Adapted from *Lillis et al.* [2008b].

variable x, where $x = 0$ at the electron's release point. As a function of x, we prescribe the magnetic elevation angle (i.e., the angle between the magnetic field vector and local horizontal), magnetic field strength $B(x)$, and electrostatic potential difference $\Delta V(x)$. We define $\Delta V(x) = 0$ when $x = 0$. Although we will set $\Delta V(x) = 0$ everywhere in all simulations in this manuscript, it is a fundamental part of the MarMCET code and is included here for completeness and consistency with *Lillis et al.* [2008b]. The evolution of the electron's pitch angle $\alpha(x)$ is given by the following equation [*Lillis et al.*, 2008b, equation 17]:

$$\sin^2\alpha(x) = \frac{B(x)}{B_0}\frac{\sin^2\alpha_0}{\left(1+\frac{e\Delta V(x)}{U_0}\right)} \quad (1)$$

At some point along the field line on which the electron is launched (i.e., for some values of x), the right-hand side of equation (1) may become ≥ 1, indicating that the pitch angle has reached 90° and hence the electron has electromagnetically reflected and is traveling in the opposite direction. This happens when either $B(x)$ grows too large (e.g., the electron is getting closer to magnetized crust) and/or when $\Delta V(x)$ gets too large and negative. Note that if the denominator becomes negative, the equation becomes meaningless, i.e., the electron cannot exist at this point x because it has already reflected. Figures 1a and 1b show a sample magnetic field profile and the resulting pitch angle evolution for electrons of several initial pitch angles.

[21] *Lillis et al.* [2008b, equation 18] describe the cumulative probability of an electron surviving the round-trip journey from some high altitude to its magnetic reflection point in the atmosphere and back again without scattering. It can be modified slightly for our purposes to express the cumulative probability of an electron colliding with an atmospheric neutral of species i, by process j (e.g., elastic collision, dissociation, ionization etc.) before traveling a distance x along the field line:

$$P_{i,j}(x) = 1 - \exp\left[-\int_0^x \frac{\sigma_{i,j}(U(x'))n_i(x')dx'}{\sqrt{1-\frac{B(x')\sin^2\alpha_0}{B_0\left(1+\frac{e\Delta V(x')}{U_0}\right)}}}, U(x')\right]$$
$$= U_0 + e\Delta V(x') \quad (2)$$

where $\sigma_{i,j}$ is the energy-dependent cross section for that process and $n_i(x)$ is the neutral density of species i as a function of x. x is represented by a 400-element array, starting at zero from an altitude of 400 km, which increases with decreasing altitude until either the electron goes below 50 km or the reflection point is reached, after which it decreases as altitude increases, reaching zero again at 400 km. Therefore the altitude resolution is always <2 km. Corresponding arrays for $n_i(x)$, $B(x)$ and $\Delta V(x)$ are calculated in order to evaluate $P_{i,j}$ as a function of x, examples of which are plotted in Figure 1d.

[22] Equation (2) is used to calculate the cumulative probability for a collision resulting in process j as a function of distance along the electron's guiding center path. A random number is used to determine where along the path,

if at all, a collision occurs. If so, the electron's position and pitch angle immediately beforehand are recorded, a second random number determines which neutral species the electron strikes according to the separate probabilities for collision with each species, and a third determines what scattering process occurs (e.g., elastic collision, dissociation, excitation or ionization) and the associated energy loss of the impacting electron, according to the relative cross sections for each process. For ionizations, the energy loss resulting from the range of possible secondary electron energies is accounted for by treating as separate processes the emission of secondaries in ~300 discrete energy bins logarithmically spaced from 0.1eV–20 keV. A fourth random number determines the polar scattering angle according to tabulated angular scattering functions (discussed in the following section) and a fifth randomly determines the azimuth scattering angle. The initial pitch angle and polar and azimuthal scattering angles determines the postcollision pitch angle. A new helical trajectory is calculated starting from the collision position, and the Monte Carlo procedure is repeated until the particle either "escapes" the atmosphere (meaning its altitude exceeds 400 km while traveling upwards) or its energy falls below 10 eV, below which it can no longer ionize atmospheric neutrals.

[23] The altitude and process of every scattering event is recorded. When an ionization occurs, a new electron is "launched" at the altitude of the collision. Its initial energy is determined by another random number, weighted by the appropriate differential cross sections (see next section), while its initial direction is chosen randomly (which results in a new pitch angle). These newly created electrons produced by electron impact are followed from their "creation," using the method just described, until either their altitude exceeds 400 km or their energy falls below the aforementioned 10 eV "further ionization" threshold. In this way, for example, we record all ~200 secondary (and tertiary etc.) electrons produced by a 20 keV primary electron precipitating through the Martian atmosphere.

2.2. Model Inputs

[24] As mentioned above, the inputs to the model are 1) electron-neutral collision cross sections, 2) the electron's initial pitch angle, 3) its initial energy, and the profiles, along the magnetic field lines to which the electron is bound, of 4) neutral density, 5) magnetic field strength and 6) electrostatic potential. We discuss these in order.

2.2.1. Cross Sections for Electron-Neutral Collisions

[25] We developed a comprehensive database of cross sections for O, O_2, N_2, CO_2, CO and Ar from *Ajello et al.* [1990], *Cvejanovic and Crowe* [1997], *Chilton and Lin* [1999], *Itikawa* [2002] and the compilation of *Sung and Fox* [2000]. Differential cross sections for secondary electron emission were obtained from *Shyn and Sharp* [1979], *Burnett and Rountree* [1979] and *Opal et al.* [1971]. Angle-dependent relative scattering cross sections were obtained from *Porter and Jump* [1978] and *Porter et al.* [1987].

2.2.2. Initial Electron Pitch Angles and Energies

[26] For every combination of crustal magnetic field and neutral density profiles in this paper, the simulation was run for 20 logarithmically spaced energies from 15 eV to 20 keV and for 12 equally spaced downward traveling pitch angle bins between 0 and $\pi/2$. Electrons below 15 eV were not considered because they do not cause ionization while those above 20 keV were not because there is very rarely any electron flux above this energy except during solar energetic particle events and because this was the highest energy of both the Mars Express ASPERA-3 ELS (ELectron Spectrometer) and the MGS MAG/ER (Magnetometer/Electron Reflectometer); that is, there are no Mars data beyond this. Simulations do not have to be run separately for different input energy spectra or PADs, since the contributions from each energy/pitch angle can be summed and weighted accordingly to predict the ionization rate profile for a given energy spectrum and PAD.

2.2.3. Atmospheric Neutral Density Profiles

[27] For all simulations in this paper, the neutral density versus altitude profiles for the six main neutral species (CO_2, O, O_2, CO, N_2, Ar) are taken from the Mars Thermospheric Global Circulation Model (MTGCM) [e.g., *Bougher et al.*, 1999] and correspond to solar moderate equatorial, equinox conditions at the equator at 0200 local time.

2.2.4. Magnetic Field Profile

[28] Since we assume the electrons are bound to a single magnetic field line, three associated one-dimensional arrays are sufficient to represent the magnetic field: altitude, magnetic field magnitude and magnetic elevation angle (i.e., angle between the magnetic field vector and the local horizontal). For simplicity, the magnetic field for all simulations in this paper is taken to be a straight line and vertical (i.e., radial) everywhere. The vertical profile of field strength is equal to the sum of a constant ambient magnetic field of 12 nT (a typical magnetotail field value [*Ferguson et al.*, 2005]) and a crustal magnetic field profile determined by its value at 100 km and which decreases with distance above the magnetized crustal source (which we assume to be 15 km beneath the surface):

$$B(z) = B_{ambient} + B_{crustal,100km} \times \left(\frac{100km}{z}\right)^{2.5} \quad (3)$$

Examples of such profiles can be seen in Figures 1a and 2b.

2.2.5. Electrostatic Potential

[29] There are two possible sources of parallel electrostatic potentials. The first is the polarization electric field due to charge separation between electrons and ions in the ambipolar diffusion region [*Schunk and Nagy*, 2000, pp 118–119]. At Mars, this occurs above ~200 km [*Withers*, 2009] and is approximately equal to kT_e/eH_p, where k is the Boltzmann constant, T_e is the electron temperature, e is the electron charge and H_p is the plasma scale height (equal to $k(T_e + T_i)/m_i g$, where m_i is the mass of the dominant ion, T_i is the ion temperature and g is the acceleration due to gravity). Putting in reasonable values for the Mars ionosphere (i.e., O_2^+ ion mass and plasma temperatures from *Hanson and Mantas* [1988]) gives an electric field of a few μV/m. Even if sustained over 200 km, such a field is too weak to affect the trajectories of the precipitating electrons.

[30] The second source is magnetospheric electrostatic potentials, up to several kilovolts, which are invoked in order to explain observations of accelerated electron spectra [*Brain et al.*, 2006] and aurora [*Bertaux et al.*, 2005]. Such potentials could exist over distances of ~1000 km [*Dubinin et al.*, 2008], mostly outside the collisional atmosphere and would

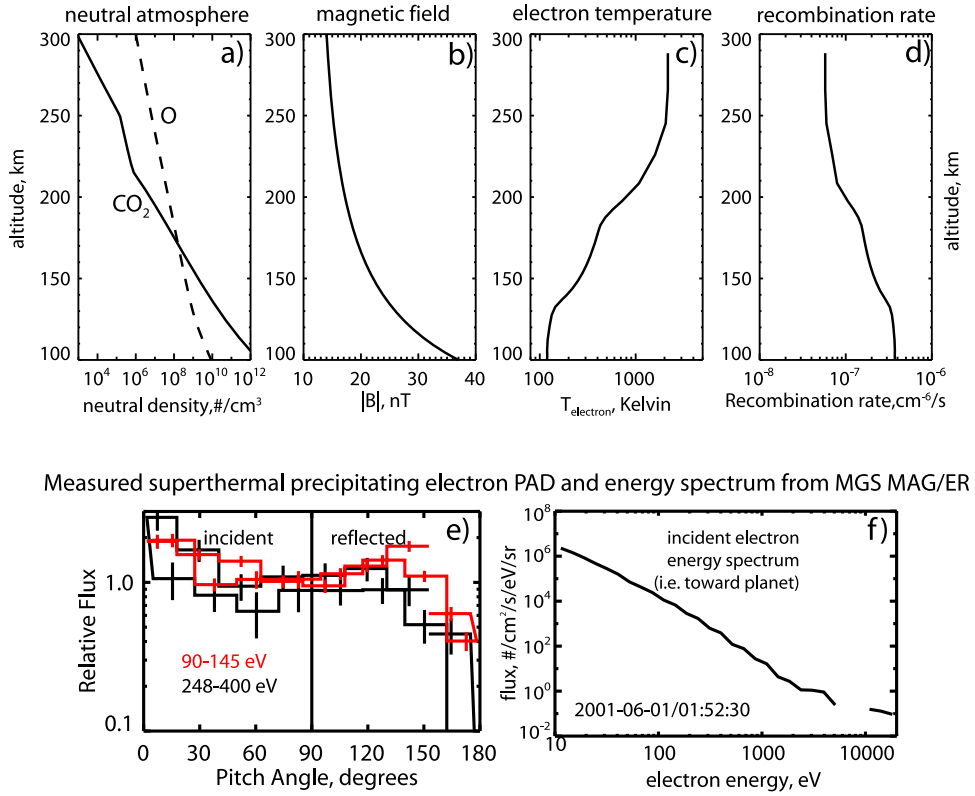

Figure 2. Typical MarMCET inputs. (top) As a function of altitude, (a) neutral atmosphere density of the two dominant constituents O and CO_2 from the MTGCM [*Bougher et al.*, 1999], (b) magnetic field magnitude of the assumed-vertical magnetic field, (c) electron temperature from *Hanson and Mantas* [1988], and (d) recombination rate for O_2^+ (the dominant ion, see section 2.4) dictated by the electron temperature. (e) Electron PADs for two sample energy channels, 90–145 eV and 248–400 eV. In the model, the overlapping pitch angle pins from the incident (left) side of the PAD are resampled to 12 nonoverlapping adjacent pitch angle bins of uniform 7.5° width. (f) The energy spectrum of the downward traveling electron flux. The measured, background-subtracted fluxes are typically at or below zero for energies above 5 keV [*Mitchell et al.*, 2001], hence the zero flux number at ~8 keV.

therefore modify the "initial" precipitating electron flux rather than its transport within the ionosphere (which is the focus of this paper). Even though it's an important part of the MarMCET code structure, we don't include electrostatic potentials in the model runs in this manuscript because there are no direct measurements of such potential at Mars and because we wish to focus on the effects of crustal magnetic field and PADs. Such potentials will be the topic of future work.

2.3. Calculating Ionization Rate

[31] For any profile of magnetic field magnitude, electrostatic potential and neutral density along a given magnetic field line, MarMCET uses all the recorded ionizations to calculate the differential ionization rate $\partial f(h, \alpha_0, U_0)/\partial h$, defined as the number of ionizations per km of altitude per primary electron of initial pitch angle α_0 and energy U_0 at altitude h. Its units are km^{-1}. Figures 3a–3c plot $\partial f(h, \alpha_0, U_0)/\partial h$ as a function of altitude and α_0 for 3 representative values of U_0 for the neutral density and magnetic field profile shown in Figures 2a and 2b.

[32] To obtain ionization rate, we must consider Gauss' Law of magnetism: as crustal magnetic field strength increases with decreasing altitude, a magnetic flux tube decreases in area to conserve magnetic flux. Therefore, the omnidirectional precipitating electron flux increases by the fractional increase in magnetic field magnitude: $B(h)/B_0$. We call this the "magnetic concentration" effect. It is illustrated qualitatively in Figure 1e by the electron's tightening helical path.

[33] The flux of downward traveling electrons is typically expressed in $cm^{-2}s^{-1}$ steradian^{-1}eV^{-1} and ionization rate is typically in units of $cm^{-3}s^{-1}$. Therefore we must not only multiply $\partial f(h, \alpha_0, U_0)/\partial h$ by $B(h)/B_0$ but also by the downward traveling flux $F(\alpha_0, U_0)$ (i.e., flux at the same α_0 and U_0) and then integrate over energy and direction to obtain ionization rate as a function of altitude $P_{ionization}(h)$. If we assume equal flux at all phase angles of the electron gyro motion (commonly referred to as "gyrotropy"), then integrating over this phase angle results in a factor of 2π: and the remaining integration is only over energy and initial pitch angle:

$$P_{ionization}(h) = 2\pi \int_0^{\frac{\pi}{2}} \int_{U_0} \frac{\partial f(h, \alpha_0, U_0)}{\partial h} \frac{B(h)}{B_0} F(\alpha_0, U_0) dU_0 d\alpha_0 \quad (4)$$

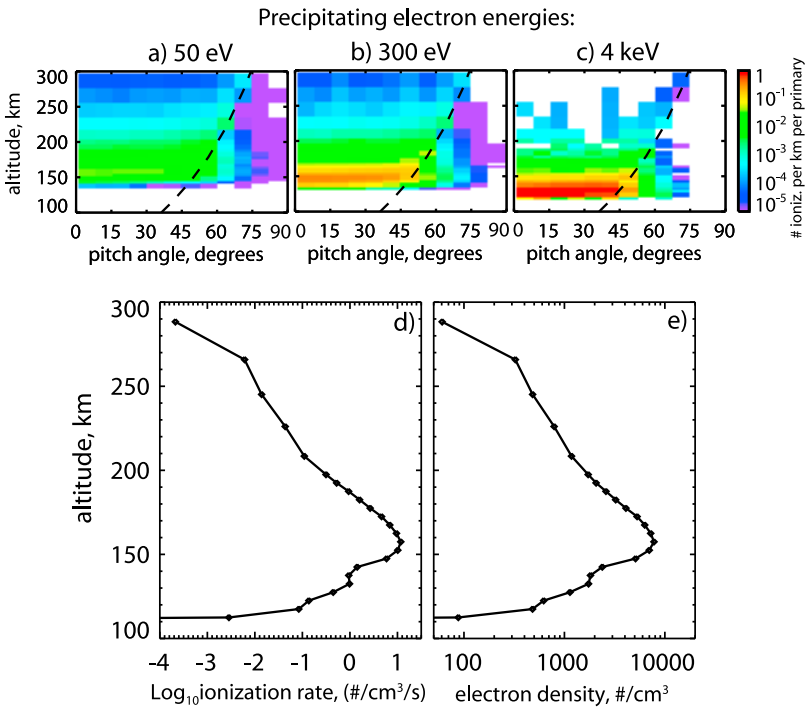

Figure 3. MarMCET outputs. (a–c) Number of ionizations per km of altitude per primary electron as a function of initial pitch angle and altitude for three sample energies. The dashed line represents the magnetic reflection altitude as a function of initial pitch angle. The small amount of ionization to the right of this line is due mostly to scattered primary electrons. (d) Resulting ionization rate profile when the electron PAD and energy spectrum from Figures 2e and 2f are run through the model. (e) Electron density profile calculated from equation (5) assuming the electron temperature and recombination rate profile shown in Figures 2c and 2d.

The number of particles simulated was varied for a given combination of energy, pitch angle and crustal magnetic field strength in order to give an approximately uniform number of ionizations, from 83 particles at 20 keV and no crustal magnetic field, to a maximum of 5 million particles at 15 eV where the reflection attitude is above 250 km, where the atmosphere is very tenuous compared to lower altitudes and ionizations consequently rare.

[34] As mentioned in section 2.1, the altitude resolution used in MarMCET (<2 km) is a small fraction of the atmospheric scale height (>8 km), so the relevant physics is captured on a particle-by-particle level. However, when aggregating all the ionizations from a given simulation run in order to calculate ionization rate as a function of altitude, we must take a large enough altitude bin size that we obtain a smoothly varying ionization rate profile. We found that this could be achieved using 24 × 5 km wide altitude bins between 80 km and 200 km, then 5 more bins with boundaries at 221, 245, 271 and 300 km.

2.4. Simplified Calculation of Electron Density

[35] For the purposes of this paper, the primary job of MarMCET is to calculate ionization rate profiles. Ideally, the profiles should be used in conjunction with a code, multifluid or otherwise, that fully takes into account neutral winds, collisions between neutrals and thermal ions and electrons, plasma diffusion and ion chemistry in order to obtain a more comprehensive picture of neutral and plasma dynamics on the Martian nightside. However, until such a code exists, we can use these rate profiles to obtain a simplified electron density for comparison to measured electron density profiles. The electron number density can be computed from the total ion production rate (ignoring dynamics and assuming photochemical equilibrium) from the equation [e.g., *Schunk and Nagy*, 2000]:

$$n_e(h) = \left[\frac{P_{ionization}(h)}{\beta_{eff}(T_e(h))}\right]^{\frac{1}{2}} \quad (5)$$

where $\beta_{eff}(T_e)$ is the electron temperature-dependent effective recombination rate in units of $cm^{-6}s^{-1}$. O_2^+ is the dominant ion in the ionosphere of Mars over the altitudes considered here due to rapid reactions between CO_2, O, and their ions [*Chen et al.*, 1978; *Hanson et al.*, 1977]. Therefore, β_{eff} is taken to be the dissociative recombination rate of O_2^+, values for which are taken from the recent work of *Sheehan and St.-Maurice* [2004] and references therein, including *Mehr and Biondi* [1969]:

$$\beta_{eff} = \left\{ \begin{array}{l} 1.95 \times 10^{-7}(300K/T_e)^{0.7}, T_e < 1200K \\ 1.73 \times 10^{-7}(300K/T_e)^{0.61}, T_e \geq 1200K \end{array} \right\}$$

In the absence of published measured or modeled nightside electron temperatures in the Mars ionosphere, we assume that the electron temperature at all altitudes is equal to the dayside electron temperature from the model of *Chen et al.* [1978],

which agrees very well with those measured by the Viking retarding potential analyzers on the dayside between 200 km and 330 km [*Hanson and Mantas*, 1988]. The altitude profiles of electron temperature and recombination rate are shown in Figures 2c and 2d. Given that the same postionization chemical processes dominate whether ionization is caused by photons or precipitating electrons, we expect this to be a more appropriate assumption than simply assuming electron temperatures equal to nightside neutral temperatures (<200K), as did *Fillingim et al.* [2007].

2.5. Model Example

[36] Figures 2 and 3 demonstrate MarMCET in the absence of electrostatic potentials. Figure 2 shows typical inputs: altitude profiles of (Figure 2a) neutral density, (Figure 2b) magnetic field, (Figure 2c) electron temperature and (Figure 2d) recombination rate. The latter two are necessary for determining electron density only, not ionization rate and are included in Figure 2 for completeness. Figures 2e and 2f show typical measured electron PADs for 2 sample energies and a downward traveling electron energy spectrum. The PAD and energy spectrum were measured by MGS MAG/ER at 0200 local time at the MGS mapping orbit altitude of ~400 km, the same altitude at which the electrons are released in the simulation.

[37] Figures 3a–3c show differential ionization rate as a function of altitude and initial electron pitch angle for 3 sample electron energies. First, it shows that, as expected, electrons of higher energy cause ionization at lower altitudes (i.e., higher neutral densities) because their collision cross sections are smaller. Also it shows that, for electrons with initial pitch angles sufficiently close to 90°, magnetic reflection plays a very important role in both raising the altitude of peak ionization and (because of exponentially lower neutral densities at higher altitudes) substantially reducing the ionization rate.

[38] Figure 3d shows the ionization rate profile resulting from the PADs and energy spectrum shown in Figures 2e and 2f, while Figure 3e shows the corresponding electron density profile, as discussed in section 2.4. The peak ionization rate occurs at 158 km, ~30 km higher than the subsolar photoionization peak. This is because photoionization cross sections are more than an order of magnitude lower than electron impact ionization cross sections in the range ~15 eV–200 eV (e.g., 1.7×10^{-17} cm^2 versus 2.7×10^{-16} cm^2 at 50 eV [*Itikawa*, 2002; *Masuoka*, 1994]), wherein lies most of the available energy for ionization in both the solar photon spectrum and the typical precipitating magnetotail electron energy spectrum. We also notice a secondary "shoulder" at ~130 km which is likely due to a slight enhancement in the energy spectrum at 4 keV (see Figure 2f). There is a notable change in slope at ~200 km caused by the larger scale height of O (versus CO_2), which dominates the neutral density above this altitude. The ionization rate in the highest altitude bin (265–300 km) is likely an artifact caused by poor statistics as the rate is expected to decrease with the atomic oxygen density.

[39] Note that, in this example, we use a constant ambient magnetic field of 12 nT and a comparatively weak crustal magnetic field of ~23 nT at 100 km. Even for this weak crustal field, downward traveling electrons with pitch angles >60° cause essentially no ionization. Crustal fields are stronger than this example over ~55% of the surface area of Mars [*Lillis et al.*, 2008a] and reach as high as ~1600 nT at 100 km in parts of Terra Cimmeria [*Acuña et al.*, 1999]. Therefore, this example shows that including the effect of magnetic gradients is essential to understanding the Mars nightside ionosphere.

3. Interconnected Effects of Crustal Magnetic Field Gradients and Electron Pitch Angle Distributions

[40] For the sake of simplicity, let us consider electron flux along an open crustal magnetic field line on the Martian nightside in the absence of electrostatic potentials. As discussed in section 2, electrons are subject to conservation of the first adiabatic invariant and so feel the so-called "mirror" force. This reduces omnidirectional electron flux as the magnetic field strength increases with decreasing altitude. However, the aforementioned "magnetic concentration" effect increases omnidirectional flux with decreasing altitude. In the absence of a collisional atmosphere and for a downward traveling electron flux which is precisely isotropic in pitch angle, these two competing effects exactly cancel each other and the electron flux remains constant with altitude [*Parks*, 2004]. However, the scattering effects of the atmospheric neutrals, as well as real, nonisotropic PADs mean that we expect to see substantial differences in vertical ionization profiles for different combinations of PADs and crustal magnetic field strengths.

[41] We used MarMCET to calculate ionization rate profiles for 3 different representative end-member PADs ("beamed" along the magnetic field line, "isotropic" and "trapped" as typically seen on closed magnetic field lines [*Brain et al.*, 2007]) and 7 different crustal magnetic field strengths. The results are shown in Figures 4 and 5. The electron energy spectrum and neutral density profile are the same as those shown in Figure 2.

[42] For the isotropic electron PAD, the flux concentration effect is smaller than the magnetic mirror effect when the scattering effect of the atmosphere is included, i.e., the ionization rates are smaller for stronger crustal magnetic field strengths, though the difference is only ~20% between the zero crustal field case and the strongest crustal field simulated.

[43] For the beamed electron PAD, where most of the flux is at pitch angles nearer 0° and hence less affected by the mirror force, the flux concentration effect dominates for higher crustal field strengths: the peak ionization rate is ~2.5 times higher for the strongest crustal field case compared to the case with crustal fields weaker than ~10 nT at 100 km.

[44] The effect of crustal magnetic field gradients is most dramatic for the trapped electron PAD. Here, the stronger the crustal field, the less ionization that is caused by the downward traveling electrons because more of them magnetically reflect before causing any substantial ionization. Peak ionization rates are an order of magnitude lower for the strongest crustal field than the zero crustal field case.

[45] Figure 5 shows how four common characteristics of ionospheres vary with PAD and crustal magnetic field strength: peak ionization rate, peak electron density ($N_{e\text{-}max}$), total electron content (TEC) and equivalent slab thickness (i.e.,

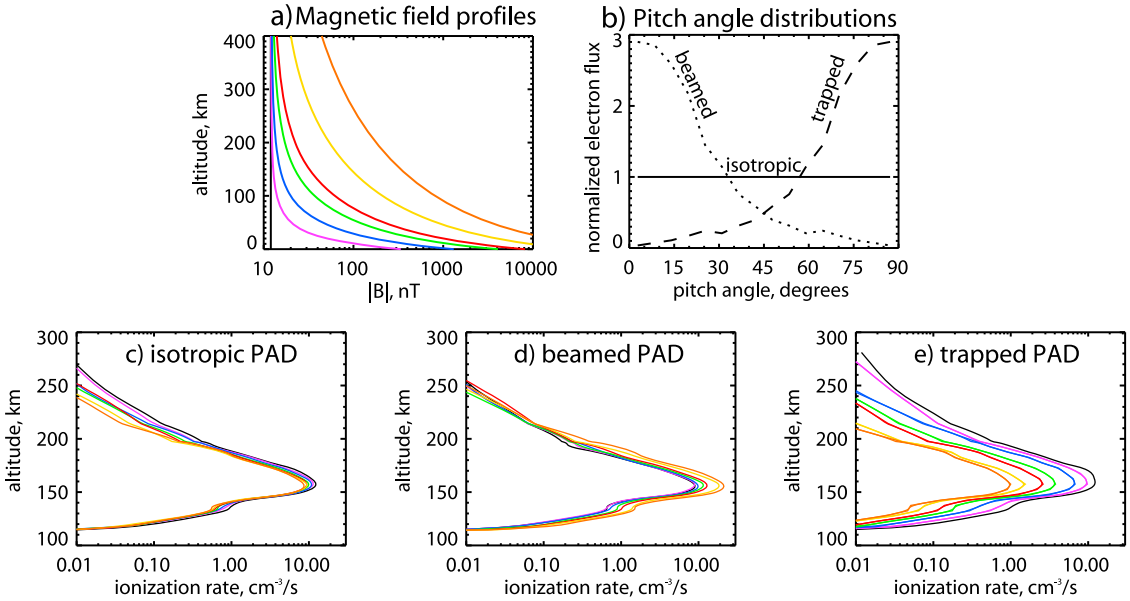

Figure 4. The coupled effects of crustal magnetic field and electron PADs on ionization rate profiles. (a and b) Input vertical magnetic field profiles and the PADs used in this series of model runs, respectively. The ambient (i.e., noncrustal) field is 12 nT for all profiles, while the colored lines correspond to crustal magnetic fields at 100 km of (black) 0.05 nT, (pink) 2 nT, (blue) 8 nT, (green) 25 nT, (red) 50 nT, (yellow) 200 nT, and (orange) 800 nT. (c–e) Vertical ionization rate profiles for all seven magnetic field profiles and three PADs. The profiles have been interpolated to 0.5 km resolution and smoothed over their intrinsic resolution of 5 km. Colors correspond to those used in Figure 4a.

TEC/$N_{e\text{-}max}$ [*Mendillo et al.*, 2004]). The precise values in these plots are not important as we chose the PADs somewhat arbitrarily. However, it is notable that, with the same electron energy spectrum, using a realistic range of crustal field strengths and just these 3 representative PADs, we obtain peak ionization rates that diverge with increasing crustal field strengths and differ by a factor of up to ~20 (Figure 5a). By equation (5), this results in peak electron densities and total electron contents (TECs) that differ by a factor of $\sim\sqrt{20} \approx 4.5$ (Figure 5b). The TEC (Figure 5c) shows a similar pattern to peak density but the equivalent slab thickness plot (Figure 5d) shows that the more beamed the PAD, the

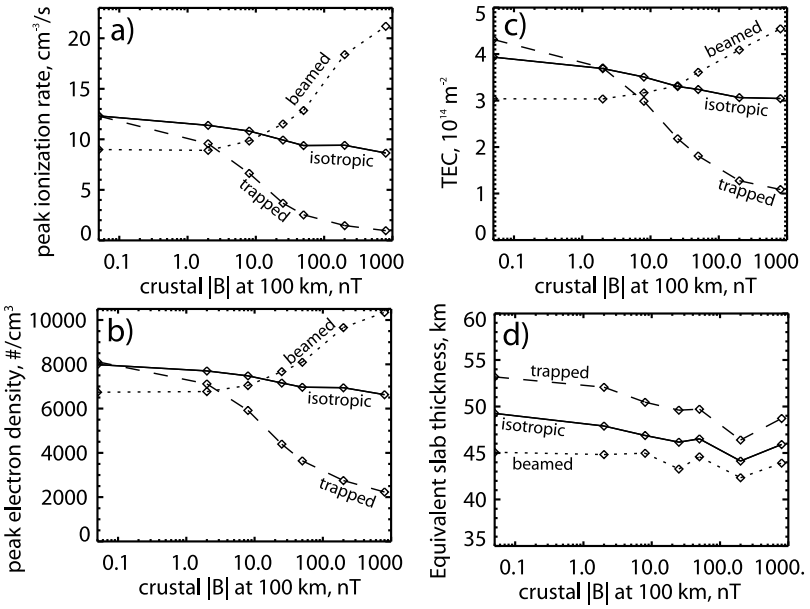

Figure 5. Plotted as a function of crustal magnetic field magnitude at 100 km: (a) peak ionization rate, (b) peak electron density, (c) total electron content (TEC), and (d) equivalent slab thickness (i.e., TEC/peak electron density). Solid, dashed, and dotted lines represent isotropic, trapped, and beamed PADs, respectively.

"thinner" the ionosphere (i.e., more of the ionosphere forms over a narrower range of altitudes). This is because electrons with pitch angles closer to 90° spend more time (and hence traverse more distance) gyrating around the magnetic field lines at higher altitudes compared with pitch angles further from 90° which reach low altitudes more quickly.

[46] One property of the vertical ionization profiles that does not seem to be much affected by crustal magnetic fields and/or electron PADs is the peak ionization altitude: it is near 160 km for all cases shown in Figure 3. This is consistent with Figures 3a–3c, which shows that peak ionization altitude is constant as pitch angle increases until ~15° below the "cut-off" pitch angle (i.e., where the reflection altitude approximately equals the exobase altitude of ~200 km), after which peak ionization rates decrease significantly.

4. Comparison With Previous Work

[47] We can compare our results to some of the Viking radio occultation and MARSIS sounder measurements mentioned in section 1, insofar as such comparisons are meaningful (i.e., we don't know the input electron spectrum, the neutral density profile or the contribution from electron transport from the dayside ionosphere). Using a typical magnetotail lobe electron energy spectrum, we found peak electron densities of ~6–8 × 10^3 cm^{-3} at ~160 km with no crustal magnetic field. This compares with typical densities of 5 × 10^3 cm^{-3} at an average peak altitude of 150 km from Viking 1 and 2 radio occultation profiles [*Zhang et al.*, 1990], as well as typical values of 8 × 10^3 cm^{-3} at an average peak altitude of 175 km from MARSIS Active Ionospheric Sounder measurements in nonmagnetic regions [*Kirchner et al.*, 2007]. The published nightside MARSIS TEC measurements of *Safaeinili et al.* [2007] show TEC = 4–6 × 10^{14} m^{-2} where crustal magnetic field lines are within 15° of vertical, compared with 1–4.5 × 10^{14} m^{-2} from MarMCET depending on PAD and crustal field strength. If we restrict ourselves to isotropic and beamed PAD (which are more likely when the magnetic field lines are nearly vertical [*Brain et al.*, 2007]), then our modeled TEC range is 3–4.5 × 10^{14} m^{-2}, so the general agreement is quite good.

[48] We can also compare to previous modeling efforts using similar input spectra. *Verigin et al.* [1991], *Haider et al.* [1992], and *Fox et al.* [1993] calculated peak electron densities of 7 × 10^3 cm^{-3}, 1.2 × 10^3 cm^{-3} and 1.4 × 10^4 cm^{-3}, respectively for magnetotail lobe spectra, which are roughly consistent with our results.

[49] Other data and model predictions for the Mars nightside ionosphere are listed by *Fillingim et al.* [2007, Table 1]. However, since we know the model results were calculated under a substantial range of input conditions and since we don't know the input conditions associated with the observations, we therefore do not consider it illuminating to compare our results to every number in that table, particularly since the purpose of this article is primarily to introduce MarMCET and investigate the effects of magnetic gradients and electron PADs.

5. Conclusions and Future Work

[50] In conclusion, we have presented MarMCET, a Monte Carlo–based electron transport code for use in planetary atmospheres. We have used it to calculate vertical profiles of electron impact ionization rates, given knowledge of 1) the energy spectrum and 2) pitch angle distribution of the precipitating electrons and the profiles of 3) magnetic field magnitude and 4) neutral density along the magnetic field lines to which the electrons are bound.

[51] We conclude that the coupled effects of crustal magnetic field gradients and electron PADs on electron impact ionization rates can be greater than a factor of 20 and should not be ignored in future modeling efforts of the Mars nightside ionosphere.

[52] We have not shown any data-model comparisons in this paper for the sake of brevity and because, due to the lack of a magnetometer on Mars Express, there do not exist simultaneous measurements of the energy spectrum and PAD of precipitating electrons and the resulting ionospheric density profile. We have also not investigated the effects of different magnetic elevation angles, seasonal and solar cycle changes in neutral density profiles, magnetic field-aligned electrostatic potentials or "peaked" (i.e., accelerated) electron spectra like those thought to cause Mars aurora [*Brain et al.*, 2006; *Bertaux et al.*, 2005]. These tasks will be left to future work.

[53] **Acknowledgments.** We wish to thank two anonymous reviewers for many helpful comments which greatly improved the manuscript. This work was supported by the NASA Mars Fundamental Research Program grant NNX09AD43G and the NASA Mars Data Analysis Program grant NNX08AK94G.

References

Acuña, M. H., et al. (1999), Global distribution of crustal magnetization discovered by the Mars Global Surveyor MAG/ER experiment, *Science*, *284*, 790–793, doi:10.1126/science.284.5415.790.

Ajello, J. M., G. K. James, B. Franklin, and S. Howell (1990), Study of electron impact excitation of argon in the extreme ultraviolet: Emission cross section of resonance lines of Ar I, Ar II, *J. Phys. B At. Mol. Opt. Phys.*, *23*, 4355–4376, doi:10.1088/0953-4075/23/23/017.

Bertaux, J.-L., F. Leblanc, O. Witasse, E. Quemerais, J. Lilensten, S. A. Stern, B. Sandel, and O. Korablev (2005), Discovery of an aurora on Mars, *Nature*, *435*, 790–794, doi:10.1038/nature03603.

Bougher, S. W., S. Engle, R. G. Roble, and B. Foster (1999), Comparative terrestrial planet thermospheres: 2. Solar cycle variation of global structure and winds at equinox, *J. Geophys. Res.*, *104*, 16,591–16,611, doi:10.1029/1998JE001019.

Bougher, S. W., S. Engel, D. P. Hinson, and J. M. Forbes (2001), Mars Global Surveyor radio science electron density profiles: Neutral atmosphere implications, *Geophys. Res. Lett.*, *28*(16), 3091–3094, doi:10.1029/2001GL012884.

Brain, D. A., J. S. Halekas, L. M. Peticolas, R. P. Lin, J. G. Luhmann, D. L. Mitchell, G. T. Delory, S. W. Bougher, M. H. Acuña, and H. Rème (2006), On the origin of aurorae on Mars, *Geophys. Res. Lett.*, *33*, L01201, doi:10.1029/2005GL024782.

Brain, D. A., R. J. Lillis, D. L. Mitchell, J. S. Halekas, and R. P. Lin (2007), Electron pitch angle distributions as indicators of magnetic field topology near Mars, *J. Geophys. Res.*, *112*, A09201, doi:10.1029/2007JA012435.

Breus, T. K., A. M. Krymskii, D. H. Crider, N. F. Ness, D. Hinson, and K. K. Barashyan (2004), Effect of the solar radiation in the topside atmosphere/ionosphere of Mars: Mars Global Surveyor observations, *J. Geophys. Res.*, *109*, A09310, doi:10.1029/2004JA010431.

Burnett, T., and S. P. Rountree (1979), Differential and total cross sections for electron-impact ionization of atomic oxygen, *Phys. Rev. A*, *20*, 1468–1473, doi:10.1103/PhysRevA.20.1468.

Chapman, S. (1931a), The absorption and dissociative or ionizing effect of monochromatic radiation in an atmosphere on a rotating Earth, *Proc. Phys. Soc. London*, *43*, 26–45, doi:10.1088/0959-5309/43/1/305.

Chapman, S. (1931b), The absorption and dissociative or ionizing effect of monochromatic radiation in an atmosphere on a rotating Earth, part ii: Grazing incidence, *Proc. Phys. Soc. London*, *43*, 483–501, doi:10.1088/0959-5309/43/5/302.

Chen, R. H., T. E. Cravens, and A. F. Nagy (1978), The Martian ionosphere in light of the Viking observations, *J. Geophys. Res.*, *83*, 3871–3876, doi:10.1029/JA083iA08p03871.

Chilton, J. E., and C. C. Lin (1999), Measurement of electron-impact excitation into the $3p^5 3d$ and $3p^5 5s$ levels of argon using Fourier-transform spectroscopy, *Phys. Rev. A*, *60*, 3712–3721, doi:10.1103/PhysRevA.60.3712.

Cvejanovic, D., and A. Crowe (1997), Differential cross sections for elastic scattering of electrons from argon and krypton as a continuous function of energy, *J. Phys. B At. Mol. Opt. Phys.*, *30*, 2873–2887, doi:10.1088/0953-4075/30/12/016.

Dubinin, E., G. Chanteur, M. Fraenz, and J. Wocha (2008), Field-aligned currents and parallel electric field potential drops at Mars: Scaling from the Earth' aurora, *Planet. Space Sci.*, *56*, 868–872, doi:10.1016/j.pss.2007.01.019.

Duru, F., D. A. Gurnett, T. F. Averkamp, D. L. Kirchner, R. L. Huff, A. M. Persoon, J. J. Plaut, and G. Picardi (2006), Magnetically controlled structures in the ionosphere of Mars, *J. Geophys. Res.*, *111*, A12204, doi:10.1029/2006JA011975.

Duru, F., D. A. Gurnett, D. D. Morgan, R. Modolo, A. F. Nagy, and D. Najib (2008), Electron densities in the upper ionosphere of Mars from the excitation of electron plasma oscillations, *J. Geophys. Res.*, *113*, A07302, doi:10.1029/2008JA013073.

Espley, J. R., W. M. Farrell, D. A. Brain, D. D. Morgan, B. Cantor, J. J. Plaut, M. H. Acuña, and G. Picardi (2007), Absorption of MARSIS radar signals: Solar energetic particles and the daytime ionosphere, *Geophys. Res. Lett.*, *34*, L09101, doi:10.1029/2006GL028829.

Espley, J. R., J. E. C. Connerney, and R. J. Lillis (2008), Effects of high energy astrophysical events on the Martian atmosphere, in *Third International Conference on the Mars Atmosphere: Modeling and Observations*, *LPI Contrib. 1447*, 9110.

Ferguson, B. B., J. C. Cain, D. H. Crider, D. A. Brain, and E. M. Harnett (2005), External fields on the nightside of Mars at Mars Global Surveyor mapping altitudes, *Geophys. Res. Lett.*, *32*, L16105, doi:10.1029/2004GL021964.

Fillingim, M. O., L. M. Peticolas, R. J. Lillis, D. A. Brain, J. S. Halekas, D. L. Mitchell, R. P. Lin, D. Lummerzheim, S. W. Bougher, and D. L. Kirchner (2007), Model calculations of electron precipitation induced ionization patches on the nightside of Mars, *Geophys. Res. Lett.*, *34*, L12101, doi:10.1029/2007GL029986.

Fox, J. L., and K. E. Yeager (2006), Morphology of the near-terminator Martian ionosphere: A comparison of models and data, *J. Geophys. Res.*, *111*, A10309, doi:10.1029/2006JA011697.

Fox, J. L., J. F. Brannon, and H. S. Porter (1993), Upper limits to the nightside ionosphere of Mars, *Geophys. Res. Lett.*, *20*(13), 1339–1342, doi:10.1029/93GL01349.

Gurnett, D. A., et al. (2005), Radar soundings of the ionosphere of Mars, *Science*, *310*(5756), 1929–1933, doi:10.1126/science.1121868.

Gurnett, D. A., et al. (2008), An overview of radar soundings of the Martian ionosphere from the Mars Express spacecraft, *Adv. Space Res.*, *41*, 1335–1346, doi:10.1016/j.asr.2007.01.062.

Haider, S. A. (1997), Chemistry of the nightside ionosphere of Mars, *J. Geophys. Res.*, *102*(A1), 407–417, doi:10.1029/96JA02353.

Haider, S. A., J. Kim, A. F. Nagy, C. N. Keller, M. I. Verigin, K. I. Gringauz, N. M. Shutte, K. Szego, and P. Kiraly (1992), Calculated ionization rates, ion densities, and airglow emission rates due to precipitating electrons in the nightside ionosphere of Mars, *J. Geophys. Res.*, *97*(A7), 10,637–10,641, doi:10.1029/92JA00317.

Haider, S. A., S. P. Seth, E. Kallio, and K. I. Oyama (2002), Solar EUV and electron-proton-hydrogen atom-produced ionosphere on Mars: Comparative studies of particle fluxes and ion production rates due to different sources, *Icarus*, *159*, 18–30, doi:10.1006/icar.2002.6919.

Haider, S. A., V. Singh, V. R. Choksi, W. C. Maguire, and M. I. Verigin (2007), Calculated densities of $H_3O^+ (H_2O)_m$, $NO_2^- (H_2O)_n$, CO_3^- (H_2O)_n and electron in the nighttime ionosphere of Mars: Impact of solar wind electron and galactic cosmic rays, *J. Geophys. Res.*, *112*, A12309, doi:10.1029/2007JA012530.

Halekas, J. S., D. A. Brain, R. J. Lillis, M. O. Fillingim, D. L. Mitchell, and R. P. Lin (2006), Current sheets at low altitudes in the Martian magnetotail, *Geophys. Res. Lett.*, *33*, L13101, doi:10.1029/2006GL026229.

Hanson, W. B., and G. P. Mantas (1988), Viking electron temperature measurements: Evidence for a magnetic field in the Martian atmosphere, *J. Geophys. Res.*, *93*, 7538–7544, doi:10.1029/JA093iA07p07538.

Hanson, W. B., S. Sanatani, and D. R. Zuccaro (1977), The Martian ionosphere as observed by the Viking retarding potential analyzers, *J. Geophys. Res.*, *82*, 4351–4363, doi:10.1029/JS082i028p04351.

Itikawa, Y. (2002), Cross sections for electron collisions with carbon dioxide, *J. Phys. Chem. Ref. Data*, *31*(3), 749–767, doi:10.1063/1.1481879.

Kirchner, D. L., D. A. Gurnett, J. D. Winningham, A. Safaeinili, J. J. Plaut, and G. Picardi (2007), Auroral ionization patches on the nightside of Mars, *Geophys. Res. Abstr.*, *9*, 04627.

Leblanc, F., J. G. Luhmann, R. E. Johnson, and E. Chassefiere (2002), Some expected impacts of a solar energetic particle event at Mars, *J. Geophys. Res.*, *107*(A5), 1058, doi:10.1029/2001JA900178.

Leblanc, F., O. Witasse, J. Winningham, D. Brain, J. Lilensten, P.-L. Blelly, R. A. Frahm, J. S. Halekas, and J. L. Bertaux (2006), Origins of the Martian aurora observed by Spectroscopy for Investigation of Characteristics of the Atmosphere of Mars (SPICAM) on board Mars Express, *J. Geophys. Res.*, *111*, A09313, doi:10.1029/2006JA011763.

Lillis, R. J., H. V. Frey, M. Manga, D. L. Mitchell, R. P. Lin, M. H. Acuna, and S. W. Bougher (2008a), An improved crustal magnetic field map of Mars from electron reflectometry: Highland volcano magmatic history and the end of the Martian dynamo, *Icarus*, *194*, 575–596, doi:10.1016/j.icarus.2007.09.032.

Lillis, R. J., D. L. Mitchell, R. P. Lin, and M. H. Acuña (2008b), Electron reflectometry in the Martian atmosphere, *Icarus*, *194*, 544–561, doi:10.1016/j.icarus.2007.09.030.

Masuoka, T. (1994), Single- and double-photoionization cross sections of carbon dioxide (CO_2) and ionic fragmentation of CO_2^+ and CO_2^{+2}, *Phys. Rev. A*, *50*, 3886–3894, doi:10.1103/PhysRevA.50.3886.

Mehr, F. J., and M. A. Biondi (1969), Electron temperature dependence of recombination of O_2^+ and N_2^+ ions with electrons, *Phys. Rev.*, *181*, 264–271, doi:10.1103/PhysRev.181.264.

Mendillo, M., X. Pi, S. Smith, C. Martinis, J. Wilson, and D. Hinson (2004), Ionospheric effects upon a satellite navigation system at Mars, *Radio Sci.*, *39*, RS2028, doi:10.1029/2003RS002933.

Mendillo, M., P. Withers, D. Hinson, H. Rishbeth, and B. Reinisch (2006), Effects of solar flares on the ionosphere of Mars, *Science*, *311*, 1135–1138, doi:10.1126/science.1122099.

Mitchell, D. L., R. P. Lin, C. Mazelle, H. Rème, P. A. Cloutier, J. E. P. Connerney, M. H. Acuña, and N. F. Ness (2001), Probing Mars' crustal magnetic field and ionosphere with the MGS Electron Reflectometer, *J. Geophys. Res.*, *106*(E10), 23,419–23,427, doi:10.1029/2000JE001435.

Molina-Cuberos, G. J., J. J. López-Moreno, R. Rodrigo, H. Lichtenegger, and K. Schwingenschuh (2001), A model of the Martian ionosphere below 70 km, *Adv. Space Res.*, *27*, 1801–1806, doi:10.1016/S0273-1177(01)00342-8.

Morgan, D. D., D. A. Gurnett, D. L. Kirchner, J. L. Fox, E. Nielsen, and J. J. Plaut (2008), Variation of the Martian ionospheric electron density from Mars Express radar soundings, *J. Geophys. Res.*, *113*, A09303, doi:10.1029/2008JA013313.

Nielsen, E., et al. (2007), Local plasma processes and enhanced electron densities in the lower ionosphere in magnetic cusp regions on Mars, *Planet. Space Sci.*, *55*, 2164–2172, doi:10.1016/j.pss.2007.07.003.

Opal, C. B., W. K. Peterson, and E. C. Beaty (1971), Measurements of secondary-electron spectra produced by electron impact ionization on a number of simple gases, *J. Chem. Phys.*, *55*, 4100–4106, doi:10.1063/1.1676707.

Parks, G. (2004), *Physics of Space Plasmas*, Westview, Jackson, Tenn.

Porter, H. S., and F. W. Jump (1978), Analytic total angular elastic electron impact cross sections for planetary atmospheres, *NASA Publ. CSC/TM-78/6017*.

Porter, H. S., F. Varosi, and H. G. Mayr (1987), Iterative solution of the multistream electron transport equation: 1. Comparison with laboratory beam injection experiments, *J. Geophys. Res.*, *92*, 5933–5959, doi:10.1029/JA092iA06p05933.

Safaeinili, A., W. Kofman, J. Mouginot, Y. Gim, A. Herique, A. B. Ivanov, J. J. Plaut, and G. Picardi (2007), Estimation of the total electron content of the Martian ionosphere using radar sounder surface echoes, *Geophys. Res. Lett.*, *34*, L23204, doi:10.1029/2007GL032154.

Schunk, R. W., and A. F. Nagy (2000), *Ionospheres: Physics, Plasma Physics, and Chemistry*, Cambridge Univ. Press, New York.

Seth, S. P., S. A. Haider, and K. I. Oyama (2002), The photoelectron flux and nightglow emissions of 5577 and 6300 Å due to solar wind electron precipitation in Martian atmosphere, *J. Geophys. Res.*, *107*(A10), 1324, doi:10.1029/2001JA000261.

Sheehan, C. H., and J.-P. St.-Maurice (2004), Dissociative recombination of N2+, O2+, and NO+: Rate coefficients for ground state and vibrationally excited ions, *J. Geophys. Res.*, *109*, A03302, doi:10.1029/2003JA010132.

Shyn, T. W., and W. E. Sharp (1979), Doubly differential cross section of secondary electrons ejected from gases by electron impact: 50–400 eV on CO_2, *Phys. Rev. A*, *20*, 2332–2339, doi:10.1103/PhysRevA.20.2332.

Sung, K., and J. L. Fox (2000), Electron impact cross sections for use in modeling the ionospheres/thermospheres of the earth and planets, *Eos. Trans. AGU*, *8148*, Fall Meet. Suppl., SA52A-11.

Tyler, G. L., G. Balmino, D. P. Hinson, W. L. Sjogren, D. E. Smith, R. A. Simpson, S. W. Asmar, P. Priest, and J. D. Twicken (2001), Radio science observations with Mars Global Surveyor: Orbit insertion through one Mars year in mapping orbit, *J. Geophys. Res.*, *106*(E10), 23,327–23,348, doi:10.1029/2000JE001348.

Ulusen, D., and I. R. Linscott (2008), Low-energy electron current in the Martian tail due to reconnection of draped interplanetary magnetic field and crustal magnetic fields, *J. Geophys. Res.*, *113*, E06001, doi:10.1029/2007JE002916.

Verigin, M. I., K. I. Gringauz, N. M. Shutte, S. A. Haider, K. Szego, P. Kiraly, A. F. Nagy, and T. I. Gombosi (1991), On the possible source of the ionization in the nighttime Martian ionosphere: 1. Phobos 2 HARPelectron spectrometer measurements, *J. Geophys. Res.*, *96*(A11), 19,307–19,313, doi:10.1029/91JA00924.

Withers, P. (2006), Mars Global Surveyor and Mars Odyssey Accelerometer observations of the Martian upper atmosphere during aerobraking, *Geophys. Res. Lett.*, *33*, L02201, doi:10.1029/2005GL024447.

Withers, P. (2009), A review of observed variability in the dayside ionosphere of Mars, *Adv. Space Res.*, *44*, 277–307.

Withers, P., and M. Mendillo (2005), Response of peak electron densities in the Martian ionosphere to day-to-day changes in solar flux due to solar rotation, *Planet. Space Sci.*, *53*, 1401–1418, doi:10.1016/j.pss.2005.07.010.

Withers, P., S. W. Bougher, and G. M. Keating (2003), The effects of topographically controlled thermal tides in the Martian upper atmosphere as seen by the MGS accelerometer, *Icarus*, *164*, 14–32, doi:10.1016/S0019-1035(03)00135-0.

Withers, P., M. Mendillo, H. Rishbeth, D. P. Hinson, and A. J. Arkani-Hamed (2005), Ionospheric characteristics above Martian crustal magnetic anomalies, *Geophys. Res. Lett.*, *32*, L16204, doi:10.1029/2005GL023483.

Zhang, M. H. G., J. G. Luhmann, and A. J. Kliore (1990), An observational study of the nightside ionospheres of Mars and Venus with radio occultation methods, *J. Geophys. Res.*, *95*, 17,095–17,102, doi:10.1029/JA095iA10p17095.

S. W. Bougher, Department of Atmospheric, Oceanic and Space Sciences, University of Michigan, 2455 Hayward St., Ann Arbor, MI 48109-2143, USA.

D. A. Brain, M. O. Fillingim, R. J. Lillis, R. P. Lin, and L. M. Peticolas, Space Sciences Laboratory, University of California, Berkeley, 7 Gauss Way, Berkeley, CA 94720, USA.